Application of surrogate models to stability analysis and transition prediction in hypersonic flows

Han Nie[1], Wenping Song[1], Zhonghua Han[1*], Guohua Tu[2] and Jianqiang Chen[2]

*Correspondence:
hanzh@nwpu.edu.cn

[1] National Key Laboratory of Science and Technology on Aerodynamic Design and Research, Northwestern Polytechnical University, Xi'an 710072, People's Republic of China
[2] China Aerodynamics Research and Development Center, Mianyang 621000, People's Republic of China

Abstract

To increase the efficiency and robustness of stability-based transition prediction in flow simulations, simplified methods are introduced to substitute direct stability analyses for rapid disturbance growth prediction. For low-speed boundary layers, these methods are mainly established based on self-similar assumptions, which are not applicable to non-similar boundary layers in hypersonic flows. The objective of this article is to investigate the application of surrogate models to stability analysis of non-similar flows over blunt cones, focused on parameterization of boundary-layer (BL) profiles. Firstly, correlations between BL edge and profile parameters are analyzed, along with self-similar flow parameters and discrete points on BL profiles, which present four groups of BL characteristic parameters. Secondly, using these parameters as inputs, surrogate models are built for disturbance growth prediction over an MF-1 blunt cone. Results show that, surrogate models using four BL edge parameters and a BL shape factor $\{U_e, T_e, \rho_e, \eta_e, H_{12}\}$ for stability analysis can achieve comparable accuracy with those using 16 discrete BL profile parameters, which are more precise than those using merely self-similar parameters or BL edge parameters. Thirdly, the established surrogate models are validated by stability analysis and transition prediction over the MF-1 blunt cone in flight experiments at the instants of $t = 17\,\mathrm{s} \sim 22\,\mathrm{s}$. Compared with direct linear stability analyses, the mean relative error of predicted disturbance growth rates by surrogate models is 8.0% and the maximum relative error of N factor envelopes is 6.6%, which indicates feasible applications of surrogate models to stability analysis and transition prediction of non-similar boundary layers in hypersonic flows.

Keywords: Surrogate models, Stability analysis, Transition prediction, Hypersonic flows, Blunt cone

1 Introduction

Laminar-to-turbulent transition of boundary layers has attracted growing concern in the aerodynamic shape design of aircrafts. For example, natural-laminar-flow design for transonic/supersonic transports needs to delay transition onset to reduce friction drag, and special thermal protection measures are required for hypersonic vehicles near transition regions, where heat fluxes increase rapidly. NASA's CFD Vision 2030 [1] regards physics-based and predictive modeling including boundary-layer transition as a basic

capability for future CFD techniques. Therefore, accurate prediction and modeling of boundary-layer transition has become a critical requirement in aerodynamic design of next-generation aircrafts.

In order to take into account flow transition in CFD simulations, many transition prediction methods have been proposed. These methods include: 1) stability-theory-based e^N method, which is a physics-based method modeling the evolution of perturbations inside boundary layers, e.g. the local linear stability theory (LST) [2–5], Bi-global LST [6], parabolized stability equations (PSE) method [7, 8] and direct numerical simulation method [9, 10]. 2) Transition criteria, which utilize empirical criteria derived from theoretical and experimental study, e.g. Arnal-Habiballah-Delcourt (AHD) criteria [11], Gleyzes criteria [12] and C1 criteria [13]. 3) Transition transport models, which implement empirical transition criteria into transport equations during flow simulation, e.g. γ-Re_θ model [14, 15], k-ω-γ model [16, 17] and amplification factor transport (AFT) model [18]. The e^N method was firstly proposed in 1956 [2] and then modified for 2D, 3D, incompressible and compressible boundary layers [19]. It has been coupled with RANS simulations and applied in boundary-layer transition prediction for airfoil/wing/wing-body configurations [20–24]. Among the existing transition prediction methods for hypersonic boundary layers, the e^N method is also one of the most widely applied and effective methods, having been calibrated by various wind tunnel and flight experiments.

While successful engineering applications of the e^N method have been devised to model the complex physics, there is still a great need to improve the efficiency and robustness of these applications [25]. For example, a common way of using the e^N method is to couple a LST solver with a RANS solver in an iterative manner [22]. The RANS solver provides boundary layer information for stability analysis. The LST solver computes growth rates and amplification factors (*N* factors) of perturbations at different frequencies and wavenumbers, and locates the transition onset where the *N* factors reach a threshold value. Coupling of the LST solver and RANS solver is implemented only after the boundary layer flow attains a level of maturity. The predicted transition location by LST is then returned to RANS simulations to substitute a former one and the turbulence models are updated accordingly. In this process, high-accuracy boundary layer profiles are needed for stability analysis, including velocity and temperature profiles, as well as their first and second derivatives [22]. This demands high-resolution flow simulations inside boundary layers, accompanied with heavy computational costs. In e^N transition prediction, a number of unstable disturbances at different frequencies and wavenumbers have to be evaluated, which also increases computation efforts. Besides, the calculation of amplification factors *N* is a non-local operation, which makes it quite difficult to implement the e^N method in a general CFD code. To convert *N* factors calculations to a local process and simplify the application of e^N method, the AFT model [17] is proposed, implementing a relation between *N* factor envelope slope and boundary-layer shape factor into transport equations. Whereas, the AFT method is mainly appropriate for low-speed flows, and further research is still necessary to extend this method for disturbance growth prediction in hypersonic flows.

As a substitute of solving linear stability equations, surrogate models are introduced to simplify the disturbance growth calculation. The application of surrogate models in linear stability analysis was firstly presented by Fuller et al. [26] in 1997, who trained

a neural network to identify the growth rates at different streamwise locations in a jet flowfiled. The predicted disturbance growth rate is very accurate with less than 2% error interpolating within the training set. In 2002, Crouch et al. [27] used neural networks to predict the growth rate of Tollmien-Schlichting (TS) waves and stationary crossflow (CF) instabilities on swept wings. Rajnarayan and Sturdza [25] introduced singular value decomposition method to describe the boundary-layer velocity and temperature profiles in the modeling of separate TS and CF modes for supersonic flows in 2013. Zafar and Xiao et al. [28] built a convolutional neural network for low-speed airfoils and found the relationship between boundary layer profiles and boundary layer shape factor. For hypersonic boundary layers, Pinna F et al. [29] selected a Gaussian basis function and used a compact support radial basis function method to predict the disturbance growth on sharp cones in 2018. Their training set was generated by stability analysis on self-similar boundary layer profiles. Danvin et al. [30, 31] investigated the accuracy of disturbance growth prediction by surrogate models on sharp cones using self-similar profiles and high-accuracy CFD profiles, respectively. Results show that surrogate models built based on self-similar profiles are more accurate than those based on CFD profiles. Whereas, Pinna and Danvin's research dealt primarily with sharp cones, where entropy layers or non-similar effects hardly exist. In 2020, Paredes et al. [32] used full CFD profiles with 61 equal-spaced points inside the boundary layer to build a convolutional neural network for stability analysis on a blunt cone. Their model can precisely predict the disturbance growth during the ascent phase of the HIFiRE-1 flight experiment. Moreover, it even outperforms direct linear stability calculations for some under-resolved basic states. Nie et al. [33] provided a surrogate-based stability analysis method for oblique first modes and Mack modes in self-similar compressible boundary layers at Mach $0 \sim 6$.

Compared with directly solving stability equations in transition prediction, using surrogate-based method is more efficient and robust. It can reduce the requirement for boundary layer resolution in CFD simulations [32], as it needs merely several characteristic BL parameters, and has the potential to be transformed into local formulations for transition transport modeling. Compared with other simplified e^N methods like e^N-envelope-fitting method and e^N-database method, a surrogate-based method can predict growth rates of separate modes at different frequencies and wavenumbers and achieve comparable accuracy to a LST method.

In general, there are two ways of parameterizing BL profiles when establishing surrogate models for disturbance growth prediction in hypersonic boundary layers. One is to describe the boundary layer using self-similar flow parameters, such as boundary-layer-edge Mach number M_e, temperature T_e and Hartree pressure gradient parameter β_H. It is suitable for sharp cones without non-similar effects, but generates some deviation for blunt cones. The other is to describe the boundary layer using discrete points on the BL profiles extracted from high-accuracy CFD results. It can deal with non-similar boundary layers and predict the disturbance growth on blunt cones with high accuracy. Whereas, this method faces the same problem as a direct linear stability analysis method, which needs high-resolution boundary layer profiles. It is also difficult to be further transformed into local formulations, which is necessary in transition transport modeling.

The objective of this article is to build surrogate models for rapid disturbance growth prediction in stability analysis and transition prediction of hypersonic boundary layers. Based on previous studies, we aim to find a proper method to describe boundary layer profiles, which is expected to be not only applicable to non-similar boundary layers near the nose of a blunt cone, but also capable of being transformed into local formulations for transition transport modeling. Instead of directly using discrete points on the boundary layer profiles by Danvin and Paredes, we have conducted correlation analyses between boundary layer flow parameters and profile parameters and found a group of characteristic parameters for boundary layer description.

This article continues in Section 3 to introduce three methods for boundary layer profile description in surrogate model training, including self-similar flow solutions, discrete point on BL profiles and correlated boundary-layer flow parameters. Section 4 presents a surrogate-based stability analysis method for hypersonic boundary layers over blunt cones. Freestream conditions are selected according to the MF-1 flight experiments. Radial basis function (RBF) models are established based on high-accuracy CFD solutions, with those characteristic BL parameters as inputs. The predicted disturbance growth rates and amplification factors for MF-1 experiments at the instants of $t = 17\,\text{s} \sim 22\,\text{s}$ by RBF models are compared with those by LST to validate the boundary layer description methods and the surrogate-based stability analysis method.

2 Theory

2.1 Linear stability theory and e^N method

To predict the transition location, linear stability theory introduces a small disturbance inside the boundary layer based on parallel flow assumption. Initial disturbances at different frequencies are located on neutral curves, where those disturbances begin to amplify. By solving linear stability equations, the disturbance growth rates are computed at each streamwise station and then integrated into an amplification factor N. The transition onset predicted by the e^N method is located where the amplification factor N reaches a pre-calibrated threshold N_{cr}. The small disturbances in linear stability theory are defined as

$$q'(x, y, t) = \hat{q}(y) \cdot e^{-\alpha_i x} e^{i(\alpha_r x - \omega t)}, \tag{1}$$

where α_r is streamwise wavenumber, α_i is streamwise growth rate, ω is circular frequency, x and y are the streamwise and normal coordinate. To compute the neutral curves or disturbance growth rates, an eigenvalue problem is solved for a given boundary layer as

$$\{\alpha_i, \alpha_r\} = f(\omega, Re_l) \ \ \text{or} \ \ \{\omega, \alpha_r\} = f(\alpha_i, Re_l), \tag{2}$$

where neutral curves are located with local Reynolds number Re_l and growth rate $\alpha_i = 0$, and disturbance growth is calculated with local Reynolds number Re_l at certain circular frequency ω. Once the disturbance growth at different frequencies is solved, amplification factors are computed along the streamwise location by

$$N = \int_{x_0}^{x} (-\alpha_i)_{fixed\,f}\,dx, \tag{3}$$

where x_0 is the location that disturbances at a certain frequency f begin to amplify. According to the transition mechanisms and disturbance parameters such as wavenumber, frequency and phase velocity, unstable disturbances can be classified as first modes (Tollmien-Schlichting waves), second modes (Mack modes) and others. The surrogate-based stability analysis method in this article is not restricted to a specific kind of unstable modes, but applies to disturbances within a range of frequencies and wavenumbers.

2.2 Radial basis function interpolation [34]

Surrogate models (or metamodels) such as kriging models, support vector machine models, neural networks and so on, have been widely used in aerodynamic design [35–37]. The RBF (radial basis function) model is one of the simplest data-driven surrogate models. Its interpolation coefficients are calculated for a given sample set based on the distances among sample points. Assuming there are n sample points $x_1, x_2, ..., x_n$ whose response values are $f_1, f_2, ..., f_n$, a system of linear equations can be obtained as

$$
\begin{bmatrix} f_1 \\ f_2 \\ \cdots \\ f_n \end{bmatrix} = \begin{bmatrix} 0 & \phi(\|x_1 - x_2\|) & \cdots & \phi(\|x_1 - x_n\|) \\ \phi(\|x_2 - x_1\|) & 0 & \cdots & \phi(\|x_2 - x_n\|) \\ \cdots & \cdots & \cdots & \cdots \\ \phi(\|x_n - x_1\|) & \phi(\|x_n - x_2\|) & \cdots & 0 \end{bmatrix} \cdot \begin{bmatrix} \lambda_1 \\ \lambda_2 \\ \cdots \\ \lambda_n \end{bmatrix}, \tag{4}
$$

where ϕ is the basis function, λ is the interpolation coefficient and $||x_i - x_j||$ is the Euclidean distance between the i-th and j-th sample points. Although the RBF model is a combination of linear equations, it can well fit complex non-linear problems with sufficient sample points. During model training, the correlation matrix sometimes meets an ill-conditioning problem, resulting from a large condition number and leading to numerical error. To avoid this problem, a regularization method is introduced by adding small values on the diagonal of the Matrix to reduce its condition number. To predict the response value of an unknown point, the distances of this point with the pre-calculated sample points are computed as inputs. The response value f_p at a new point x_p is predicted as

$$f_p = \sum_{j=1}^{n} \phi\left(\|x_p - x_j\|\right) \cdot \lambda_j. \tag{5}$$

The basis function in this article is a thin-plate spline function, which is $\phi(r) = r^2 \log r$.

3 Boundary layer description methods

As mentioned above, solving the eigenvalue problem for disturbance growth rate requires detailed BL information, including velocity and temperature profiles as well as their derivatives. According to the convergence study by Fischer et al. [22], at least 60 or more points are needed inside the boundary layer to ensure the accuracy of stability analysis. To represent the full BL profile, a few characteristic parameters are usually introduced. For example, a single parameter of BL shape factor H_{12} can be used to characterize a low-speed boundary layer on a flat plate or airfoil, as the BL flow shows

self-similar characteristics. When it comes to hypersonic boundary layers on blunt cones, the blunt nose results in off-body shock waves and entropy layers, which could bring non-similar effects to BL profiles. To find a proper BL description method for such non-similar boundary layers, three kinds of BL characteristic parameters are investigated, which are self-similar flow parameters, discrete points on BL profile and correlated BL flow parameters.

3.1 Self-similar flow parameters

Solution of self-similar profiles on a sharp cone at zero angle of attack refers to [38]. Firstly, the boundary layer equations of a sharp cone in polar coordinate are given as

$$
\begin{aligned}
&\frac{\partial \rho U}{\partial r} + \frac{1}{r}\frac{\partial \rho V}{\partial \theta} + \frac{2\rho U}{r} = 0 \\
&\rho\left(U\frac{\partial U}{\partial r} + \frac{1}{r}V\frac{\partial U}{\partial \theta}\right) = \frac{1}{r^2}\frac{\partial}{\partial \theta}\left(\mu\frac{\partial U}{\partial \theta}\right) \\
&\rho\left(U\frac{\partial h}{\partial r} + \frac{1}{r}V\frac{\partial h}{\partial \theta}\right) = \frac{1}{r^2}\frac{\partial}{\partial \theta}\left(\frac{\mu}{Pr}\frac{\partial h}{\partial \theta}\right) + \frac{\mu}{r^2}\left(\frac{\partial U}{\partial \theta}\right)^2,
\end{aligned}
\tag{6}
$$

where r and θ are polar coordinates as shown in Fig. 1, h is enthalpy, U and V are streamwise and normal velocities, ρ is density, μ is dynamic viscosity, and Pr is Prandtl number. Applying a transformation of $\eta = r(\theta - \theta_0)/\sqrt{r}$ and $\overline{V} = V \cdot \sqrt{r}$, where θ_0 is the cone angle, the boundary layer equations are reduced to a system of total differential equations as

$$
\begin{aligned}
&-\frac{\eta}{2}\frac{d\rho U}{d\eta} + \frac{d\rho \overline{V}}{d\eta} + 2\rho U = 0 \\
&\left(\frac{U}{2}\eta + \overline{V}\right)\rho\frac{dU}{d\eta} = \frac{d}{d\eta}\left(\mu\frac{dU}{d\eta}\right) \\
&\left(\frac{U}{2}\eta + \overline{V}\right)\rho\frac{dh}{d\eta} = \frac{d}{d\eta}\left(\frac{\mu}{Pr}\frac{dh}{d\eta}\right) + \mu\left(\frac{dU}{d\eta}\right)^2.
\end{aligned}
\tag{7}
$$

To resolve the "$2\rho U$" terms in the continuity equation, an additional transformation of $\tilde{\eta} = \sqrt{3}\eta$ and $\overline{V} = \sqrt{3}\left(\tilde{V} - 2/3 \cdot \tilde{\eta}U\right)$ is introduced. After this, the boundary layer equations of a sharp cone are converted to the same formulation as that of a flat plate. As a result, the similarity solutions of sharp-cone boundary layer equations can be obtained as on a flat plate, which refers to [39]. Considering the pressure gradient over cone surface, solving the similar equations requires only boundary-layer edge Mach number M_e, temperature T_e and Hartree parameter β_H ($\beta_H = \frac{2m}{m+1}, m = \frac{\xi}{u_e}\frac{du_e}{d\xi}, \xi = \int_0^{x_s} \rho_e u_e \mu_e dx_s$). Therefore, according to similar solutions on sharp cones, a parameter set $\{M_e, T_e, \beta_H\}$
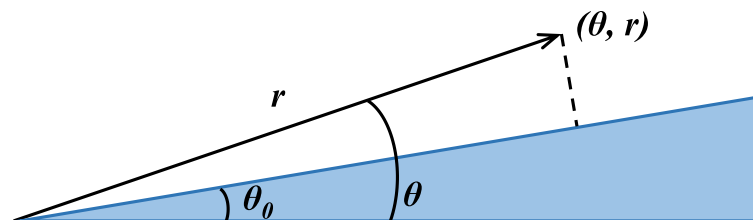

Fig. 1 Diagram of polar coordinate system on a sharp cone

(a) velocity   (b) velocity derivative   (c) temperature   (d) temperature derivative
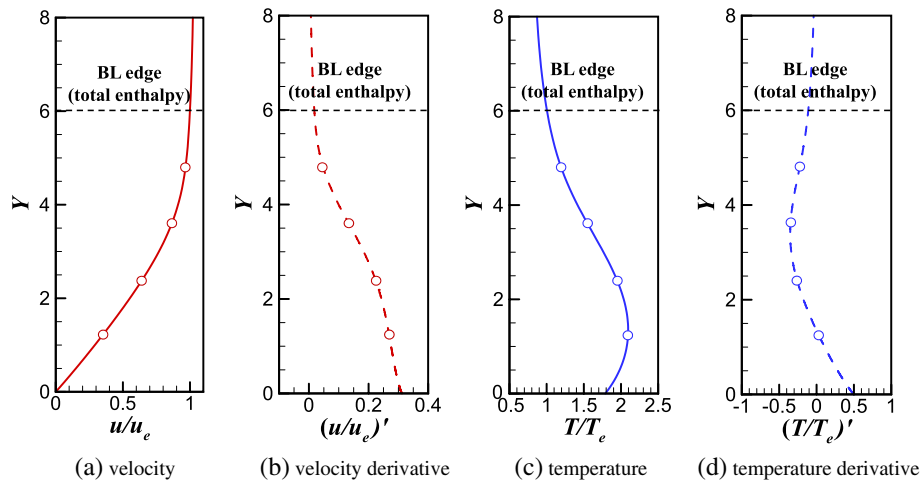
Fig. 2 Discrete points extracted from BL profiles on blunt cones with BL edge located by total enthalpy

(marked as A) is used as the inputs of MODEL A for surrogate model training in the next section.

3.2 Discrete boundary-layer profile parameters

It has been proved by [32] that using self-similar profiles generates some deviation from the CFD profiles on blunt cones. To consider the non-similar effects, a simple method is to use discrete points inside boundary layers to represent BL profiles. As an example, the velocity and temperature value as well as their derivatives are extracted at four equal-spaced locations on the BL profiles in Fig. 2. This parameter set $\{(u/u_e)_{0.2\delta},\ (u/u_e)_{0.4\delta},\ (u/u_e)_{0.6\delta},\ (u/u_e)_{0.8\delta},\ (u/u_e)'_{0.2\delta},\ (u/u_e)'_{0.4\delta},\ (u/u_e)'_{0.6\delta},\ (u/u_e)'_{0.8\delta},\ (t/t_e)_{0.2\delta},\ (t/t_e)_{0.4\delta},\ (t/t_e)_{0.6\delta},\ (t/t_e)_{0.8\delta},\ (t/t_e)'_{0.2\delta},\ (t/t_e)'_{0.4\delta},\ (t/t_e)'_{0.6\delta},\ (t/t_e)'_{0.8\delta}\}$ (marked as B) will be used as the inputs of MODEL B for surrogate model training in the next section.

3.3 Correlated boundary-layer flow parameters

According to self-similar boundary layer solutions, BL edge flow parameters are highly correlated to BL profiles. Although using self-similar parameters is not enough to represent non-similar boundary layers on blunt cones, additional BL edge parameters can be included to increase accuracy. Those non-similar effects originate from off-body shock waves and entropy layers near the blunt cone nose, which are mainly influenced by freestream Mach number M_∞ and nose radius of cone [40]. Therefore, we conducted correlation analyses between BL edge and profile parameters based on CFD simulations over blunt cone at different freestream Mach numbers and different nose radiuses. In this study, the positions of BL edge are defined between the maximum-enthalpy point and farfield, where local enthalpy reaches the average value of maximum-enthalpy and freestream enthalpy, as depicted in Fig. 3.

3.3.1 Correlation of BL parameters at different freestream Mach numbers M∞

With fixed nose radius of 5 mm, boundary layer flows of blunt cones are computed at freestream Mach numbers from $M_\infty = 4$ to $M_\infty = 6$. The half cone angle is 7°,
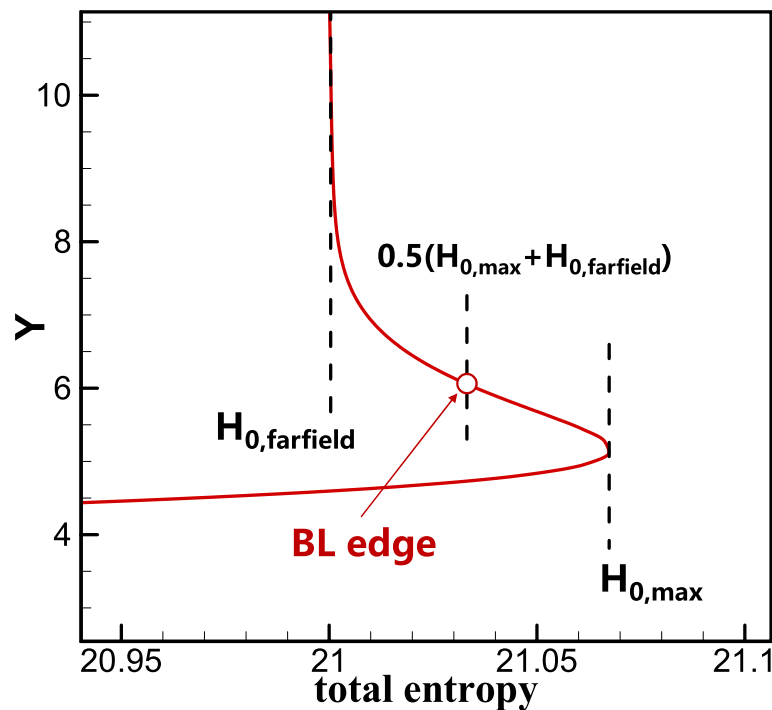
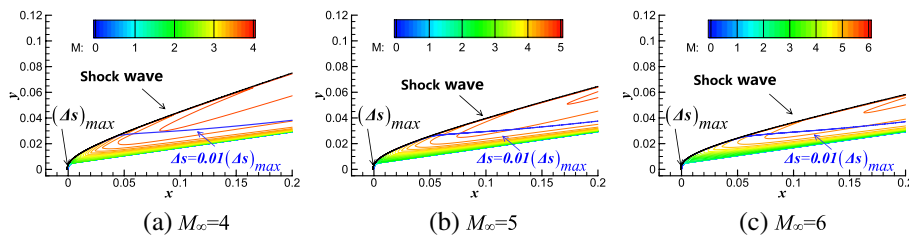**Fig. 3** Definition of boundary-layer edge by total enthalpy

Fig. 4 Flow field of blunt cones at different freestream Mach numbers

freestream Mach number is selected at $M_\infty = 4$, 4.2, 4.4, ..., 6.0, unit Reynolds number is $Re_\infty = 2 \times 10^7/\text{m}$ and angle of attack is 0°. Referring to [40], the entropy layer edge is defined at the location where local entropy production reaches 0.01 times the maximum entropy production at stagnation point. The Mach number contour and entropy layer edge distributions at different Mach numbers are presented in Fig. 4. It can be seen that the location of entropy layer edge hardly moves with the increase of Mach number, but the absolute value of entropy production inside the entropy layer is larger. The pressure distribution at BL edge is also given in Fig. 5, which shows that the absolute value of pressure increases with the Mach number, but its relative distribution varies only a little. Correlation analyses are conducted between BL flow parameters using BL data at $s = 0.2\,\text{m} \sim 1.0\,\text{m}$ for all the freestream conditions. Using the extracted characteristic BL parameters and BL profile parameters, the square Pearson correlation coefficients are computed by
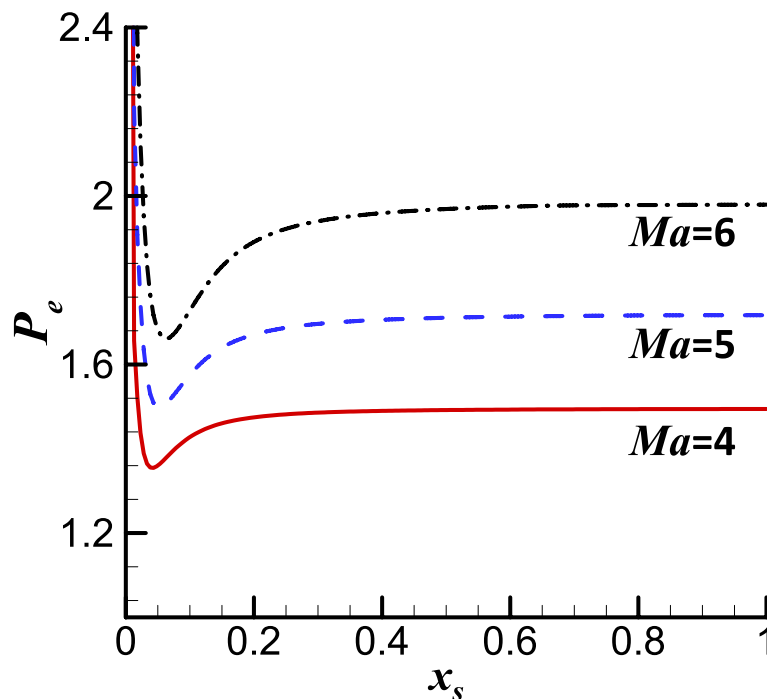
Fig. 5 Pressure distribution along streamwise coordinate x_s of blunt cones at different freestream Mach numbers

$$C_{square\ Pearson} = \frac{\sum\limits_{i=1}^{n} \left[(x_i - \bar{x})(y_i - \bar{y}) \right]^2}{\sum\limits_{i=1}^{n} (x_i - \bar{x})^2 \sum\limits_{i=1}^{n} (y_i - \bar{y})^2}, \tag{8}$$

where x_i is the characteristic boundary layer parameter of the i-th profile, y_i is the boundary layer profile parameter of the i-th profile, $\bar{x}$ and $\bar{y}$ are the averaged values, respectively. It is shown in Tables 1 and 2 that velocity profiles are most related with s_e, T_e, η_e, H_{12} and β_H, while temperature profiles are correlated with ρ_e and u_e. Furthermore, the entropy production s_e can be computed using T_e and ρ_e. The shape factor H_{12} is usually estimated by Mach number M_e and Hartree pressure gradient factor β_H. Therefore, the parameter set $\{U_e, T_e, \rho_e, \eta_e, \beta_H\}$ (marked as C) and $\{U_e, T_e, \rho_e, \eta_e, H_{12}\}$ (marked as D) are expected to be appropriate for BL profiles over blunt cones at different Mach numbers. Note that parameter set C only uses BL edge parameters, while set D includes an integral BL shape factor. These two parameter sets will be validated to see if they are suitable for blunt cones with different nose radiuses.

3.3.2 Correlation of BL parameters at different nose radiuses RN

With fixed freestream Mach number at $M_\infty = 5$, boundary layer flows are computed for blunt cones with nose radiuses from $r_n = 2\,\mathrm{mm}$ to $r_n = 8\,\mathrm{mm}$. The half cone angle is 7°, freestream Mach number is $M_\infty = 5.0$, unit Reynolds number is $Re_u = 2 \times 10^7/\mathrm{m}$ and angle of attack is 0°. The Mach number contour and entropy layer edge distributions at different nose radiuses are presented in Fig. 6. It can be seen that the absolute value of entropy

Table 1 Correlation matrix of BL flow parameters with velocity profiles at different freestream Mach numbers

	$(u/u_e)_{0.2\delta}$	$(u/u_e)_{0.4\delta}$	$(u/u_e)_{0.6\delta}$	$(u/u_e)_{0.8\delta}$	$(u/u_e)'_{0.2\delta}$	$(u/u_e)'_{0.4\delta}$	$(u/u_e)'_{0.6\delta}$	$(u/u_e)'_{0.8\delta}$
M_e	0.0009857	0.0007744	4.23e-05	0.1959	0.8238	0.2581	0.0294	0.05286
U_e	0.1836	0.1468	0.1852	0.5063	0.5277	0.5345	0.3073	0.3797
S_e	0.6615	0.7263	0.7672	0.2845	0.2567	0.1485	0.5806	0.5867
P_e	0.2199	0.1836	0.2327	0.5329	0.4269	0.5216	0.3462	0.4323
T_e	0.7388	0.7895	0.8482	0.4054	0.1255	0.2531	0.6965	0.7234
ρ_e	0.2518	0.3146	0.3131	0.006733	0.6867	0.001375	0.1566	0.1364
η_e	0.7314	0.6597	0.5792	0.6338	0.277	0.9917	0.7799	0.6488
H_{12}	0.817	0.8056	0.6509	0.2446	0.009751	0.5017	0.6843	0.4577
β_H	0.7303	0.7754	0.7303	0.3124	0.1967	0.2157	0.5836	0.5066

Table 2 Correlation matrix of BL flow parameters with temperature profiles at different freestream Mach numbers

	$(t/t_e)_{0.2\delta}$	$(t/t_e)_{0.4\delta}$	$(t/t_e)_{0.6\delta}$	$(t/t_e)_{0.8\delta}$	$(t/t_e)'_{0.2\delta}$	$(t/t_e)'_{0.4\delta}$	$(t/t_e)'_{0.6\delta}$	$(t/t_e)'_{0.8\delta}$
M_e	0.6365	0.6866	0.6364	0.7346	0.692	0.2215	0.3454	0.3373
U_e	0.1899	0.2365	0.1979	0.3235	0.8463	0.001385	0.02896	0.02594
S_e	0.7188	0.6681	0.7033	0.5433	0.002167	0.8798	0.8733	0.8916
P_e	0.1261	0.1725	0.1406	0.2568	0.8618	0.002467	0.009994	0.00784
T_e	0.5445	0.4859	0.5247	0.3592	0.04906	0.8123	0.7541	0.7724
ρ_e	0.9948	0.9825	0.9725	0.8926	0.1784	0.7795	0.8715	0.8751
η_e	0.0008498	0.0003664	0.005479	0.001981	0.1784	0.06062	0.1258	0.1065
H_{12}	0.2963	0.3949	0.444	0.3312	0.03864	0.317	0.658	0.5921
β_H	0.6198	0.6611	0.7078	0.6195	0.02168	0.6665	0.8628	0.8544

(a) $R_n=2$ mm (b) $R_n=5$mm (c) $R_n=8$mm
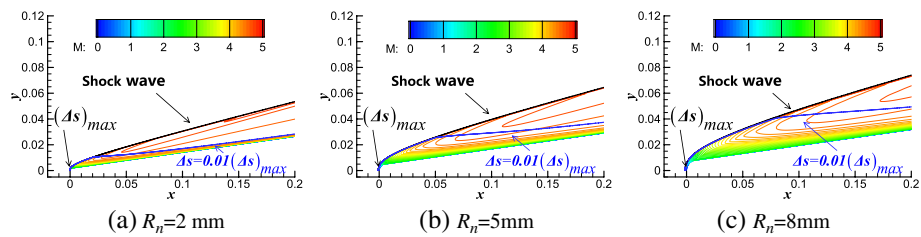
Fig. 6 Flow field of blunt cones at different nose radiuses
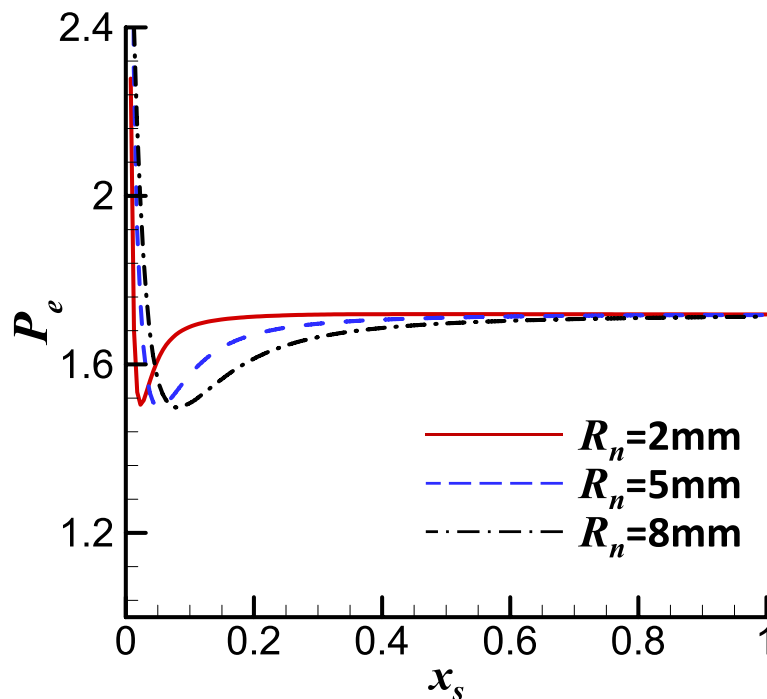
Fig. 7 Pressure distribution along streamwise coordinate x_s of blunt cones at different nose radiuses

Table 3 Correlation matrix of BL flow parameters with velocity profiles at different nose radiuses

	$(u/u_e)_{0.2\delta}$	$(u/u_e)_{0.4\delta}$	$(u/u_e)_{0.6\delta}$	$(u/u_e)_{0.8\delta}$	$(u/u_e)'_{0.2\delta}$	$(u/u_e)'_{0.4\delta}$	$(u/u_e)'_{0.6\delta}$	$(u/u_e)'_{0.8\delta}$
M_e	0.2822	0.27	0.188	0.04453	0.7586	0.138	0.03568	0.005048
U_e	0.237	0.2245	0.1508	0.04014	0.8341	0.19	0.0152	0.0003368
S_e	0.2234	0.211	0.1396	0.04081	0.8486	0.204	0.01101	6.63e-06
P_e	0.3675	0.358	0.2997	0.035	0.5248	0.03988	0.08884	0.06184
T_e	0.2365	0.2238	0.1492	0.04446	0.8322	0.1893	0.01524	0.000241
ρ_e	0.3085	0.2966	0.2118	0.03968	0.7162	0.1123	0.05027	0.01078
η_e	0.3898	0.4079	0.4795	0.5987	0.4875	0.9832	0.7533	0.7538
H_{12}	0.7017	0.7153	0.7462	0.4942	0.1782	0.8173	0.9357	0.8255
β_H	0.2433	0.2367	0.1963	0.02114	0.555	0.08583	0.03332	0.02445

production changes very little with nose radius, but the location of entropy layer edge moves outward. The pressure distribution at BL edge is also given in Fig. 7. Pressures experience the effects of upstream bluntness right up to a surface length of about $s = 0.5$, beyond which point they settle down to a uniform value. In the bluntness region, the absolute pressure values diminish with bluntness past the minimum value. Correlation analyses are conducted between BL parameters using BL data at $s = 0.2\,\mathrm{m} \sim 1.0\,\mathrm{m}$ for all the nose radiuses. The computed square Pearson correlation coefficients are listed in Tables 3 and 4. It can be seen that the relationship between velocity profiles and H_{12} is still close, so is that between

Table 4 Correlation matrix of BL flow parameters with temperature profiles at different nose radiuses

	$(t/t_e)_{0.2\delta}$	$(t/t_e)_{0.4\delta}$	$(t/t_e)_{0.6\delta}$	$(t/t_e)_{0.8\delta}$	$(t/t_e)'_{0.2\delta}$	$(t/t_e)'_{0.4\delta}$	$(t/t_e)'_{0.6\delta}$	$(t/t_e)'_{0.8\delta}$
M_e	0.9987	0.9801	0.9147	0.7614	0.1649	0.9294	0.8563	0.6758
U_e	0.9739	0.9441	0.8704	0.7728	0.1872	0.9076	0.7833	0.6091
S_e	0.9637	0.9305	0.8541	0.7671	0.1944	0.9008	0.7619	0.5883
P_e	0.6455	0.686	0.702	0.8223	0.01346	0.5024	0.613	0.5826
T_e	0.9789	0.9482	0.8728	0.7658	0.1905	0.9154	0.7885	0.61
ρ_e	0.9973	0.9866	0.9291	0.7609	0.1469	0.9228	0.8833	0.7071
η_e	0.09537	0.02802	0.0002787	0.003376	0.8763	0.2178	0.006565	0.07601
H_{12}	0.0004322	0.02788	0.09735	0.1256	0.7242	0.02819	0.1587	0.3114
β_H	0.5833	0.5969	0.5922	0.7209	0.03821	0.4762	0.494	0.4582

Table 5 Four sets of parameters for boundary layer profile description

Mark	Source	Parameters for boundary layer description
A	Self-similar solutions	M_e, T_e, β_H
B	Discrete points	$(u/u_e)_{0.2\delta}$, $(u/u_e)_{0.4\delta}$, $(u/u_e)_{0.6\delta}$, $(u/u_e)_{0.8\delta}$, $(u/u_e)'_{0.2\delta}$, $(u/u_e)'_{0.4\delta}$, $(u/u_e)'_{0.6\delta}$, $(u/u_e)'_{0.8\delta}$, $(t/t_e)_{0.2\delta}$, $(t/t_e)_{0.4\delta}$, $(t/t_e)_{0.6\delta}$, $(t/t_e)_{0.8\delta}$, $(t/t_e)'_{0.2\delta}$, $(t/t_e)'_{0.4\delta}$, $(t/t_e)'_{0.6\delta}$, $(t/t_e)'_{0.8\delta}$
C	Correlation analysis	U_e, T_e, ρ_e, η_e, β_H
D	Correlation analysis	U_e, T_e, ρ_e, η_e, H_{12}

temperature profiles and ρ_e and u_e. But the correlation factor between velocity profiles and other parameters becomes much lower, which can influence the effects of parameter set C. We will further use the parameter sets C and D as inputs in training surrogate models in the next section to see which of them is more accurate.

3.4 Brief summary of BL characteristic parameters

In Section 3, three methods are discussed for BL profile description, including using self-similar flow parameters, discrete BL profile parameters and correlated BL flow parameters. As a result, four sets of parameters (marked as A, B, C and D) are derived as inputs in establishing surrogate models for stability analysis over blunt cones, which are summarized in Table 5. To further study the accuracy of the four parameter sets A ~ D in stability analysis modeling, surrogate models A ~ D using those parameters as inputs will be investigated in Section 4.

4 Surrogate-based stability analysis on MF-1 blunt cone at flight experiments [41]

Based on four sets of characteristic parameters, surrogate models are established for stability analysis over MF-1 blunt cone at flight experiments [41]. The main purpose of using surrogate models is to substitute linear stability solvers for rapid

disturbance-growth prediction. Apart from better efficiency and robustness, the surrogate-based method also removes the necessity of high-resolution boundary layer solutions, which can reduce the computational cost of CFD simulations and has the potential to be further implemented in transition transport modeling.

The process of building surrogate models in this article is described as follows. Firstly, a database is generated by performing CFD simulations and stability analyses on MF-1 blunt cones at different freestream conditions. Secondly, characteristic flow parameters are extracted as input of surrogate models, along with the disturbance parameters. Thirdly, the complete sample set is partitioned into smaller sample sets and RBF models are trained for each sub-set. Finally, the trained RBF models are used in stability analysis and transition prediction. The flow charts of disturbance growth prediction by direct linear stability analysis and by surrogate models are depicted in Fig. 8, respectively.

4.1 Database generation

Considering the non-similarity of hypersonic boundary layers on blunt cones, it's difficult to establish a universal surrogate model like in low-speed boundary layers over flat plates or airfoils. The objective of using surrogate models is thus to satisfy the requirement of disturbance growth prediction in transition prediction within a particular range of configurations and freestream conditions. In this article, the MF-1
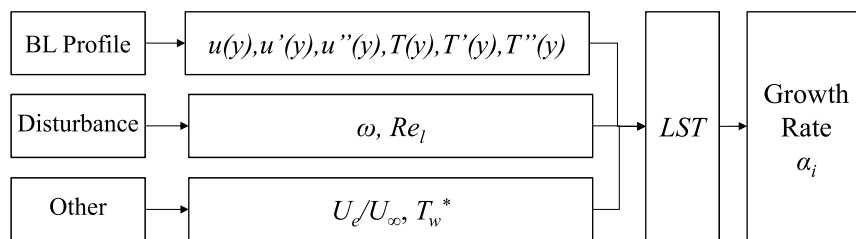
(a) Direct linear stability analysis
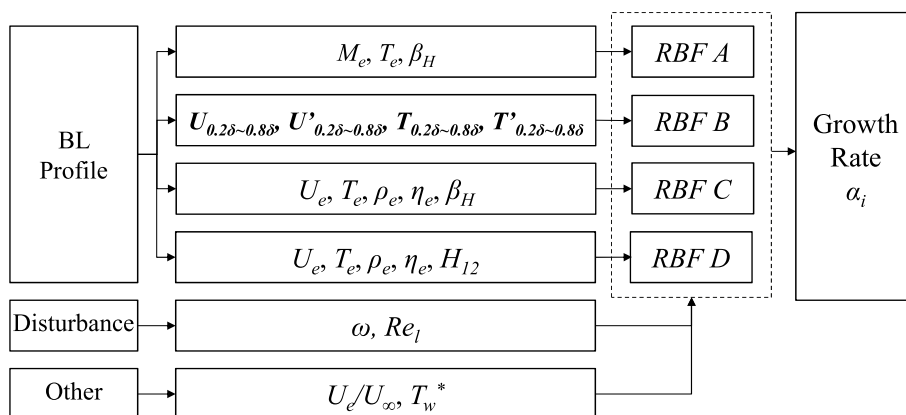
(b) Surrogate models

Fig. 8 Diagram of disturbance growth rate prediction by direct linear stability analysis and surrogate models

Table 6 Parameters of MF-1 flight experiment at ascent phase

t/s	H/km	M_∞	Re_∞/m^{-1}	T_w/K	T_∞/K
17	11.20	4.54	3.333×10^7	518	216.65
18	12.24	4.87	3.036×10^7	531	216.65
19	13.35	5.23	2.739×10^7	575	216.65
20	14.50	5.25	2.295×10^7	595	216.65
21	15.63	5.08	1.860×10^7	595	216.65
22	16.71	4.93	1.524×10^7	600	216.65

Table 7 Parameters of baseflow calculation of samples for training surrogate models

Parameter	Range	Interval	Sampling levels
M_∞	$4.3 \sim 5.5$	0.2	7
Re_∞/m^{-1}	$1.4 \times 10^7 \sim 3.5 \times 10^7$	0.3×10^7	8
T_w/K	$500 \sim 600$	25	5
T_∞/K	216.65	/	1

blunt cone [41] during ascent phase at flight experiments is chosen to validate the surrogate-based stability analysis method. Its half cone angle is 7° and nose radius is 5 mm. Freestream conditions of the MF-1 cone at flight experiments are listed in Table 6.

In order to satisfy the above condition, flow parameters for calculating training samples are selected at Mach numbers $M_\infty = 4.3$: 0.2: 5.5, unit Reynolds number $Re_\infty = 1.4 \times 10^7$: 0.3×10^7: 3.5×10^7 and wall temperatures $T_w = 500$: 25: 600, as listed in Table 7, which add up to 280 base flows. The computational states of the MF-1 flight experiment can be interpolated from the training samples, as shown in Fig. 9. The base flows are computed using a Laminar NS solver using a second order up-wind scheme. The BL profiles are extracted for linear stability analysis. Characteristic BL profile and edge parameters are also extracted according to the four groups of sample sets A ~ D.

Based on the extracted BL information, a linear stability solver is adopted to compute the growth rates α_i of perturbations at non-dimensional circular frequency of $\omega = 0 \sim 1.0$ at all the streamwise locations. An example of the computed growth rate contour at different frequencies is demonstrated in Fig. 10. Although the physical frequency of unstable modes varies a lot at different streamwise directions, it is observed that the neutral curves of all the unstable modes in the training sample set are located within the range of non-dimensional circular frequency of $0.38 < \omega < 0.72$ and local Reynolds number of $Re_l > 2000$. To cater for possible disturbance growth rates remaining below zero, stability analysis results are extracted at 31 circular frequencies from $\omega = 0.35$ to $\omega = 0.75$ and 31 streamwise locations at $Re_l > 1800$.

Finally, growth rates of disturbance at the 31 frequencies and 31 streamwise locations for 280 freestream conditions are used as response values in the training samples, together with the A, B, C, D four sets of boundary layer parameters and disturbance parameters as input values, which add up to 269,080 sample points.
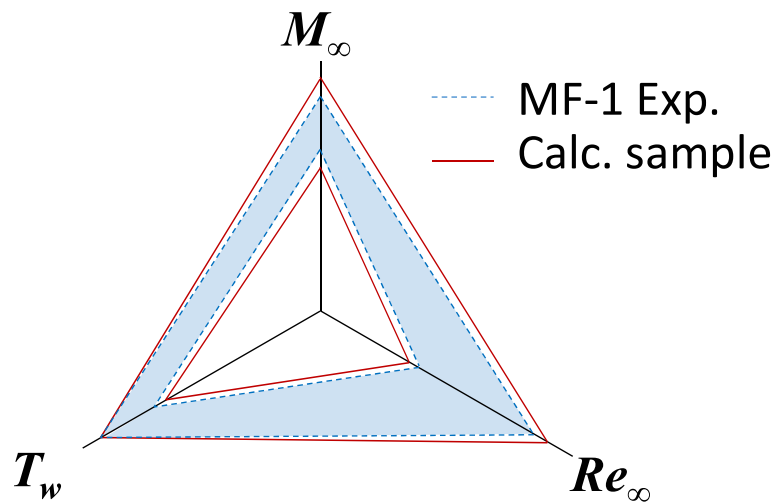
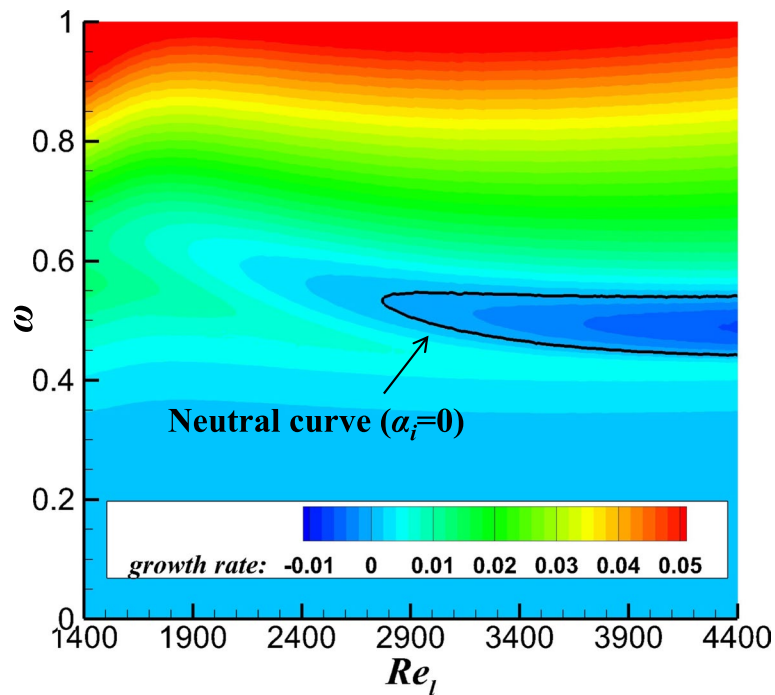**Fig. 9** Parameter range of MF-1 flight experiment and calculated training samples

Fig. 10 Computed growth rates and neutral curve of MF-1 case at $t = 21\,\mathrm{s}$

4.2 Surrogate model training

RBF models with thin-plate spline basis function are established to predict disturbance growth. Considering the difficulties of model training brought about by a large number of sample points, a sample partition method is utilized to classify the complete sample set into a series of sub sample sets. Thus, models are trained within each of the sub-sample-sets. When used for prediction, the validation samples also need to search for their corresponding sub-sample-set and surrogate model. Based on this idea, the database with 269,080 sample points is partitioned into 25 sub-sets. In the 25 partitions (5×5), five are selected on the basis of non-dimensional frequency, and the other five are based

$\omega \times 5$	1~7	7~13	13~19	19~25	25~31
$Re_l \times 5$	1~7	7~13	13~19	19~25	25~31

Fig. 11 Partition of sample points by non-dimensional frequency and local Reynolds number

(a) t=17s, Re_l=4700   (b) t=18s, Re_l=4400   (c) t=19s, Re_l=4100

(d) t=20s, Re_l=3800   (e) t=21s, Re_l=3500   (f) t=22s, Re_l=3200
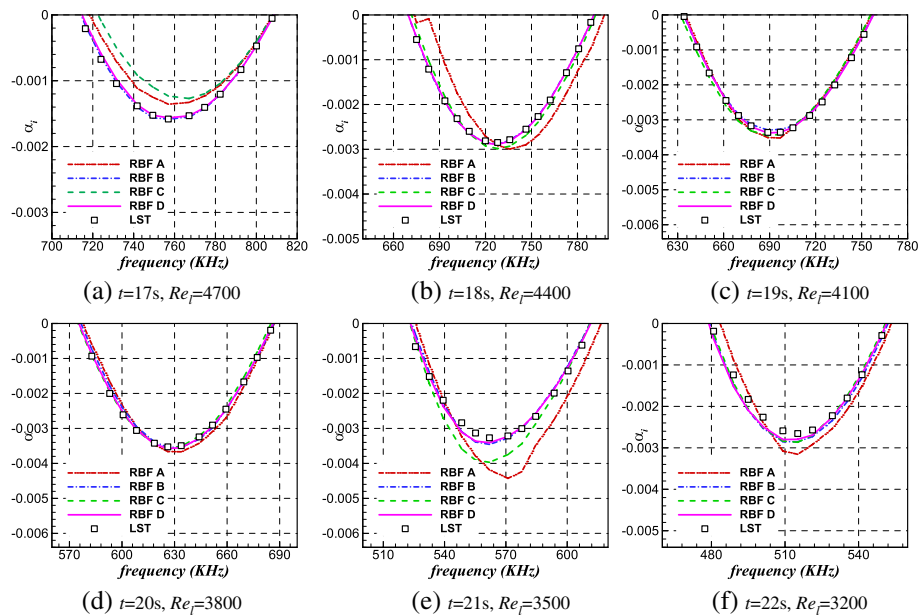
Fig. 12 Comparison of predicted growth rates by LST and RBF models at different instants for MF-1 experiment

on local Reynolds number criteria (as shown in Fig. 11). The number of sample points within each of the sample set is near 12,000. Using the four sets of characteristic parameters A, B, C and D, RBF models are trained (also marked as A, B, C and D) and their prediction accuracies are compared in Section 4.3.

4.3 Comparison of prediction accuracy of RBF models using different input parameters

To assess the accuracy of the four sets of surrogate models, validated samples are selected by stability analysis on MF-1 blunt cones at the instants of $t = 17\,\text{s} \sim 22\,\text{s}$ during ascent of flight experiments. Predicted growth rates are compared with those computed by linear stability analysis. Firstly, the computed disturbance growth rate at different frequencies at the moment of $t = 17\,\text{s} \sim 22\,\text{s}$ by those RBF models and by LST are compared in Fig. 12. It can be seen that the predicted values by RBF model B and D agree well with those by LST, while the results of RBF A and C show some deviations. The relative errors of all validation samples using the four RBF models have been gathered and listed in Table 8. It is demonstrated that RBF models using 16 discrete BL profile parameters (models B) and using four BL edge parameters and a shape factor (models D) are the most accurate. They are obviously more precise than those using self-similar flow parameters (models A) and using merely BL edge parameters (models C). As expected, the mere use of self-similar profiles or BL

Table 8 Comparison of prediction errors of growth rates by RBF models A ~ D on MF-1 blunt cone

RBF Model	Mean Absolute Error	Mean Square Error	Mean Relative Error	R^2
A	0.169×10^{-3}	0.743×10^{-7}	43.4%	0.9984
B	0.886×10^{-4}	0.336×10^{-7}	8.3%	0.9993
C	0.116×10^{-3}	0.403×10^{-7}	29.1%	0.9991
D	0.657×10^{-3}	0.209×10^{-7}	8.0%	0.9996
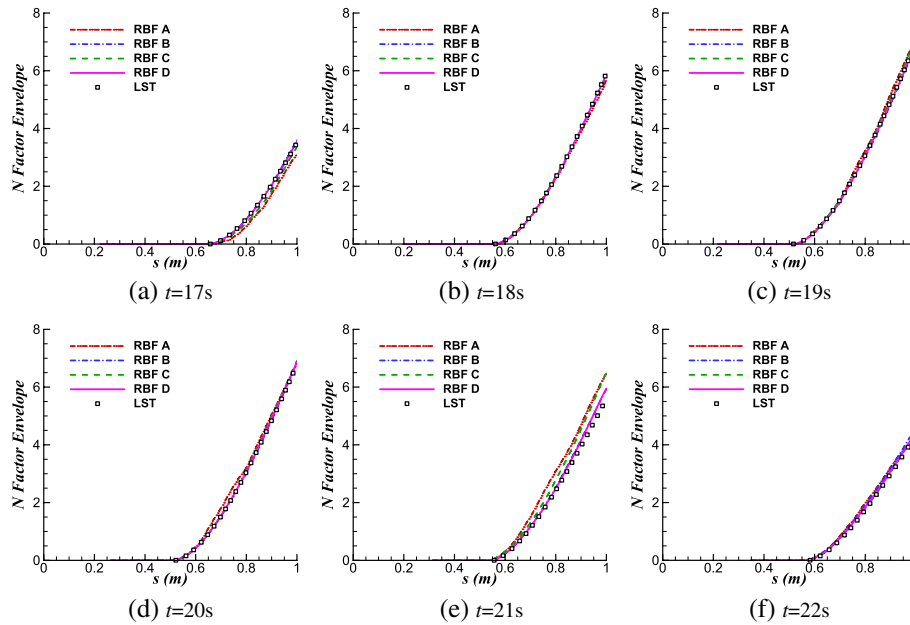
Fig. 13 Comparison of *N* factor envelopes by LST and RBF models at different instants for MF-1 experiment

edge parameter to describe BL profiles overlooks the non-similar effects in blunt cone boundary layers, which can lead to deviation from realistic BL profiles. The *N* factor envelopes computed by LST and RBF models are also compared at different stream-wise locations, as shown in Fig. 13. It can be seen that, regardless of the deviations in predicted growth rates, the RBF models using self-similar parameters and BL edge parameters can still provide reasonable prediction for *N* factors. While RBF models using discrete profile parameters and those using BL edge parameters and shape factor are more accurate, especially at $t = 17\,\mathrm{s}$ and $t = 21\,\mathrm{s}$.

4.4 Validation of RBF models using BL characteristic parameters in stability analysis and transition prediction

It has been shown in Section 4.3 that RBF models using merely four BL edge parameters and a shape factor can be as accurate as those using 16 discrete BL profile parameters. In view of the potential that BL edge parameters and shape factor can be converted into local variables and used for transition transport modeling, we would like to further investigate the accuracy of RBF models with those parameters in boundary layer stability analysis and transition prediction.

The contours and distributions of predicted disturbance growth rates by RBF models D (using four BL edge parameters and a shape factor as inputs) are compared with those by LST in Fig. 14. As can be seen from the figure, the predicted growth rate of RBF models D at instants from $t = 17\,\text{s}$ to $t = 22\,\text{s}$ agrees well with those by LST, which means that the established models D are applicable to non-similar boundary layers on hypersonic blunt cones. Computational costs of the two methods are also given in Table 9. To predict growth rates of a group of disturbances at different frequencies and streamwise locations (3600 samples in total), RBF models take only 13.38 s, while the LST method requires about 877.32 s. The reason for saving time cost by surrogate-based method is that it uses pre-calculated results to interpolate the growth rates, while the direct linear stability analysis method needs to solve the stability equations iteratively.

The amplification factors of disturbances on MF-1 blunt cones are also computed by RBF D models and the LST method, respectively. As shown in Fig. 15, the N factors at different frequencies and their envelopes computed by RBF D models are very close to those by the LST method. The maximum relative error of N factor envelope is 6.6%, demonstrating the accuracy of disturbance growth prediction using RBF models with four BL edge parameters and a shape factor for non-similar blunt cone boundary layers. It also shows that the established surrogate models are a good substitute for directly solving stability equations in e^N transition prediction.

5 Conclusion

To improve the efficiency and robustness of e^N transition prediction, we have investigated application of surrogate-based stability analysis for non-similar boundary layers, focused on input parameters for boundary-layer (BL) profile description. Four sets of BL parameters are proposed as input parameters for establishing surrogate models. The accuracies of these models are validated through MF-1 flight experiments and compared with direct linear stability analysis. Some conclusions are obtained as follows.

(1) The proposed surrogate-based method can substitute direct stability analysis for rapid disturbance growth prediction on hypersonic blunt cones. It can increase the efficiency of e^N transition prediction, which gets rid of the necessity of high-resolution BL profiles, initial eigenvalue search and iterative solution of stability equations. Because the surrogate models merely use BL edge parameters and shape factor, they also have the potential to be transformed into local formulations and implemented in transition transport models for general CFD applications.

(2) Correlation analyses demonstrate that BL edge parameters and shape factor are highly correlated with BL profiles. Surrogate models using merely four BL edge parameters and a shape factor $\{U_e, T_e, \rho_e, \eta_e, H_{12}\}$ for stability analysis and transition prediction can achieve comparable accurate results with those using 16 discrete boundary layer profile parameters.
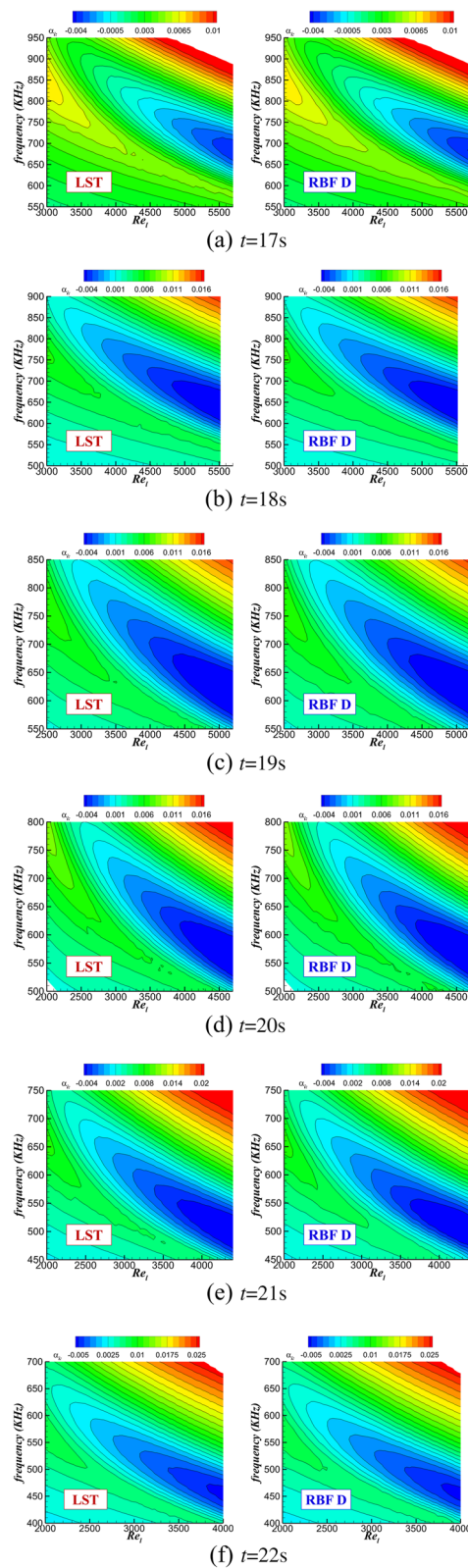
Fig. 14 Comparison of predicted disturbance growth-rate contours and surfaces by LST and RBF D at different instants for MF-1 experiment

Table 9 Comparison of time cost in a singular evaluation by LST and RBF D for MF-1 experiment (CPU: i7−2600 3.4GHz)
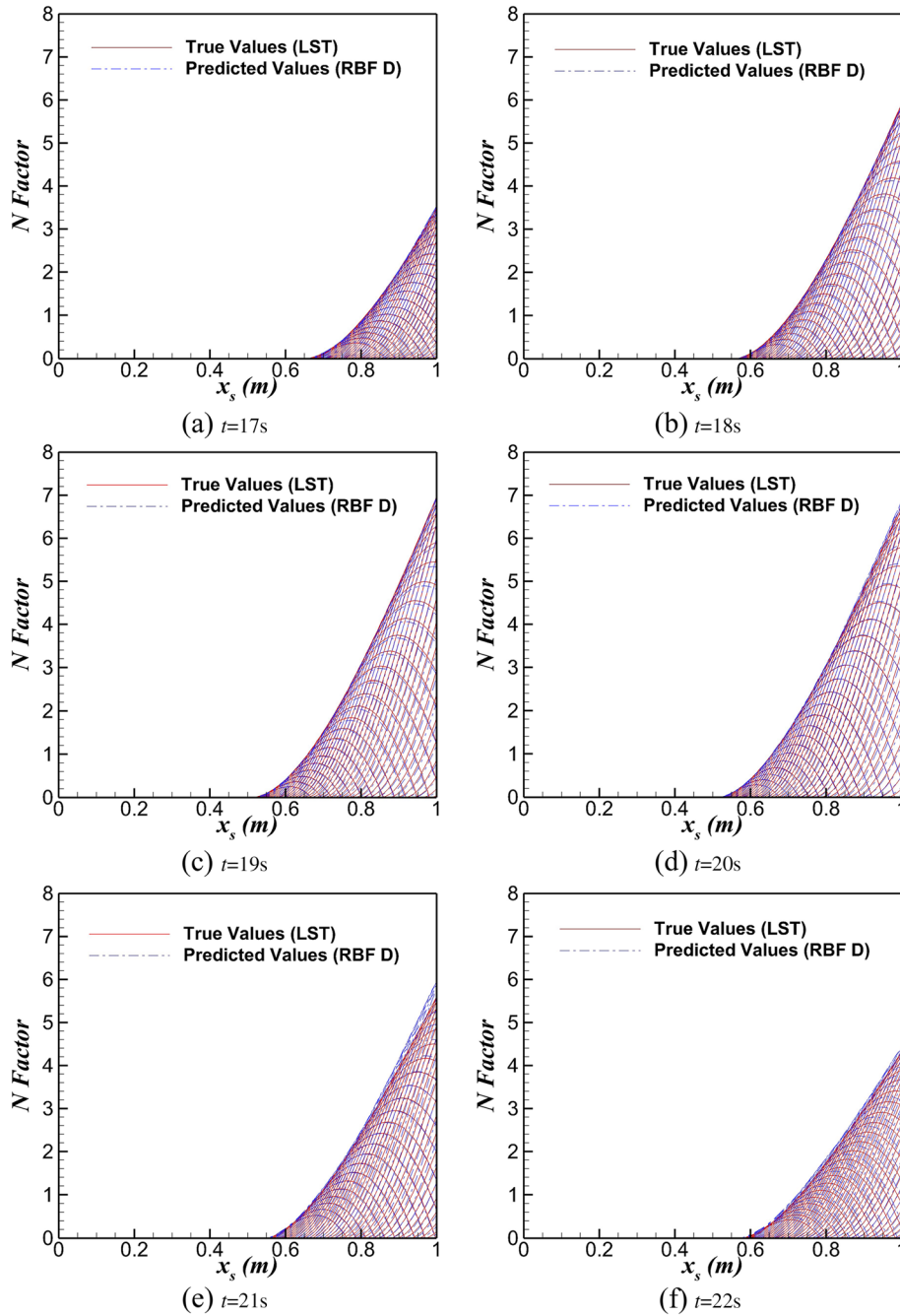
Method	Computational time
LST	877.32 s
RBF D	13.38 s

Fig. 15 Comparison of computed *N* factors by LST and RBF D at different instants for MF-1 flight experiment

(3) For MF-1 blunt cone at flight experiments, the mean relative error of predicted disturbance growth rates by established surrogate models is 8.0% and the maximum relative error of calculated N factor envelopes is less than 6.6%, which validates the applicability of surrogate-based methods using merely BL edge parameters and shape factor to stability analysis and transition prediction of non-similar boundary layers over blunt cones.

References
1. Slotnick JP, Khodadoust A, Alonso J et al (2014) CFD vision 2030 study: a path to revolutionary computational aerosciences. NASA Contractor Report NASA/CR-2014-218178. https://ntrs.nasa.gov/citations/20140003093
2. Smith AMO, Gamberoni N (1956) Transition, pressure gradient and stability theory. Douglas Aircraft Company Report No. ES 26388, El Segundo, 31 August 1956
3. Saric WS (1994) Physical description of boundary-layer transition: experimental evidence. AGARD special course on progress in transition modelling, 19940029379. https://ntrs.nasa.gov/citations/19940029379
4. Arnal D (1994) Boundary-layer transition: predictions based on linear theory. AGARD special course on progress in transition modelling, Rept 793
5. Mack LM (1984) Boundary-layer linear stability theory. AGARD special course on stability and transition of laminar flow, 19840025688. https://ntrs.nasa.gov/citations/19840025688
6. Theofilis V (2003) Advances in global linear instability analysis of nonparallel and three-dimensional flows. Prog Aerosp Sci 39:249–315. https://doi.org/10.1016/S0376-0421(02)00030-1
7. Kosarev L, Séror S, Lifshitz Y (2016) Parabolized stability equations code with automatic inflow for swept wing transition analysis. J Aircraft 53(6):1647–1669. https://doi.org/10.2514/1.C033509
8. Herbert T (1997) Parabolized stability equations. Annu Rev Fluid Mech 29(1):245–283 https://www.annualreviews.org/doi/10.1146/annurev.fluid.29.1.245
9. Dong SW, Chen JQ, Yuan XX et al (2020) Wall pressure beneath a transitional hypersonic boundary layer over an inclined straight circular cone. Adv Aerodyn 2,29. https://doi.org/10.1186/s42774-020-00057-4
10. Qi H, Li XL, Yu CP et al (2021) Direct numerical simulation of hypersonic boundary layer transition over a lifting-body model HyTRV. Adv Aerodyn 3,31. https://doi.org/10.1186/s42774-021-00082-x
11. Arnal D, Casalis G, Houdeville R (2008) Practical transition prediction methods: subsonic and transonic flows. NATO Research & Technology Organisation (RTO), Educational Notes, EN-AVT-151, June 2008
12. Gleyzes C, Cousteix J, Bonnet JL (1985) Theoretical and experimental study of low Reynolds number transitional separation bubbles. In: Proceedings of the conference on low Reynolds number airfoil aerodynamics, University of Notre Dame, Notre Dame, June 1985, pp 137–152
13. Arnal D, Houdeville R, Séraudie A et al (2011) Overview of laminar-turbulent transition investigations at ONERA Toulouse. AIAA paper 2011-3074. https://doi.org/10.2514/6.2011-3074
14. Menter FR, Langtry RB, Likki SR et al (2006) A correlation-based transition model using local variables—part I: model formulation. J Turbomach 128(3):413–422. https://doi.org/10.1115/1.2184352
15. Langtry RB, Sengupta K, Yeh DT et al (2015) Extending the γ-Re$_{\theta t}$ local correlation based transition model for crossflow effects. Paper presented at the 45th AIAA fluid dynamics conference, Dallas, 22-26 June 2015, AIAA 2015-2474. https://doi.org/10.2514/6.2015-2474
16. Wang L, Fu S (2011) Development of an intermittency equation for the modeling of the supersonic/hypersonic boundary layer flow transition. Flow Turbul Combust 87(1):165–187. https://doi.org/10.2514/6.2015-2474

17. Xiang XH, Chen JQ, Yuan XX et al (2022) Cross-flow transition model predictions of hypersonic transition research vehicle. Aerosp Sci Technol 122:107327. https://doi.org/10.1016/j.ast.2022.107327

18. Pascal L, Delattre G, Deniau H et al (2020) Stability-based transition model using transport equations. AIAA J 58(7):2933–2942. https://doi.org/10.2514/1.J058906

19. Saric WS, Reed HL, White EB (2003) Stability and transition of three-dimensional boundary layers. Annu Rev Fluid Mech 35:413–440. https://doi.org/10.1146/annurev.fluid.35.101101.161045

20. Krumbein A, Krimmelbein N, Grabe C (2017) Streamline-based transition prediction techniques in an unstructured computational fluid dynamics code. AIAA J 55(5):1548–1564. https://doi.org/10.2514/1.J054990

21. Perraud J, Arnal D, Casalis G et al (2009) Automatic transition predictions using simplified methods. AIAA J 47(11):2676–2684. https://doi.org/10.2514/1.42990

22. Fischer JS, Soemarwoto BI, van der Weide ETA (2021) Automatic transition prediction in a Navier–Stokes solver using linear stability theory. AIAA J 59(7):2409–2426. https://doi.org/10.2514/1.J059910

23. Han ZH, Chen J, Zhang KS et al (2018) Aerodynamic shape optimization of natural-laminar-flow wing using surrogate-based approach. AIAA J 56(7):2579–2593. https://doi.org/10.2514/1.J056661

24. Xu ZM, Han ZH, Chi JB et al (2021) Crossflow instability analysis for swept laminar flow wings using crossflow pressure gradient. AIAA J 59(8):2878–2889. https://doi.org/10.2514/1.J059971

25. Rajnarayan D, Sturdza P (2013) Extensible rapid transition prediction for aircraft conceptual design using modal decomposition. AIAA paper 2013-0231. https://doi.org/10.2514/6.2013-231

26. Fuller RM, Saunders W, Vandsburger U (1997) Neural network estimation of disturbance growth using a linear stability numerical model. AIAA paper 1997-559. https://doi.org/10.2514/6.1997-559

27. Crouch JD, Crouch IWM, Ng LL (2002) Transition prediction for three-dimensional boundary layers in computational fluid dynamics applications. AIAA J 40(8):1536–1541. https://doi.org/10.2514/2.1850

28. Zafar MI, Xiao H, Choudhari MM et al (2020) Convolutional neural network for transition modeling based on linear stability theory. Phys Rev Fluids 5:113903. https://arxiv.org/abs/2005.02599

29. Pinna F, Zanus L, Demange S et al (2018) Reduced model for transition prediction in hypersonic flows. Paper presented at the 2018 fluid dynamics conference, Atlanta, 25-29 June 2018, AIAA 2018-3697. https://doi.org/10.2514/6.2018-3697

30. Danvin F, Olazabal-Loumé M, Pinna F (2018) Laminar to turbulent transition prediction in hypersonic flows with metamodels. Paper presented at the 2018 fluid dynamics conference, Atlanta, 25-29 June 2018, AIAA 2018-3701. https://doi.org/10.2514/6.2018-3701

31. Danvin F, Olazabal-Loumé M, Pinna F (2019) Laminar to turbulent transition prediction in hypersonic flows with neural networks committee. Paper presented at the AIAA aviation 2019 forum, Dallas, 17-21 June 2019, AIAA 2019-2837. https://doi.org/10.2514/6.2019-2837

32. Paredes P, Venkatachari B, Choudhari MM et al (2020) Toward a practical method for hypersonic transition prediction based on stability correlations. AIAA J 58(10):4475–4484. https://doi.org/10.2514/1.J059407

33. Nie H, Song WP, Han ZH et al (2022) A surrogate-based e^N method for compressible boundary-layer transition prediction. J Aircraft 59(1):89–102. https://doi.org/10.2514/1.C036377

34. Buhmann MD (2000) Radial basis functions. Acta Numer 9:1–38. https://doi.org/10.1017/S0962492900000015

35. Han ZH, Xu CZ, Zhang L et al (2020) Efficient aerodynamic shape optimization using variable-fidelity surrogate models and multilevel computational grids. Chinese J Aeronaut 33(1):31–47. https://doi.org/10.1016/j.cja.2019.05.001

36. Han ZH, Zhang Y, Xu CZ et al (2019) Aerodynamic optimization design of large civil aircraft wings using surrogate-based model. Acta Aeronaut Astronaut Sin 40(1):522398 (Chinese)

37. Liu J, Song WP, Han ZH et al (2017) Efficient aerodynamic shape optimization of transonic wings using a parallel infilling strategy and surrogate models. Struct Multidisc Optim 55(3):925–943. https://doi.org/10.1007/s00158-016-1546-7

38. Hantzsche W, Wendt H (1941) Die laminare Grenzschicht bei einem mit überschallgeschwindigkeit angestr?mten nichtangestellten Kreiskegel. Jahrbuch der Deutschen Luftfahrtforschung 1: 76-77. (German)

39. Schlichting H (1979) Boundary-layer theory, 7th edn. McGraw Hill, New York

40. Ou JH, Wan BB, Liu JX et al (2018) Basic flow characteristics in entropy layer of hypersonic flow around blunt body. Acta Aerodyn Sin 36(2):238–246. (Chinese). https://doi.org/10.7638/kqdlxxb-2018.0032

41. Tu GH, Wan BB, Chen JQ et al (2019) Investigation on correlation between wind tunnel and flight for boundary layer stability and transition of MF-1 blunt cone. Sci Sin Phys Mech Astron 49(12):124701. (Chinese). https://doi.org/10.1360/SSPMA-2019-0162

Publisher's Note